21st IAEA Fusion Energy Conference
Chengdu, China, 16 - 21 October, 2006

IAEA-CN-149/ EX/3-2

Density Regime of Complete Detachment and Operational Density Limit in LHD

J. Miyazawa et al.

NIFS-836 Oct. 2006

EX/3-2

Density Regime of Complete Detachment and Operational Density Limit in LHD

J. Miyazawa 1), R. Sakamoto 1), S. Masuzaki 1), B.J. Peterson 1), N. Tamura 1), M. Goto 1), I. Yamada 1), K. Narihara 1), K. Tanaka 1), T. Tokuzawa 1), M. Shoji 1), M. Kobayashi 1), H. Arimoto 2), K. Kondo 2), S. Murakami 3), H. Funaba 1), S. Sakakibara 1), M. Osakabe 1), S. Morita 1), Y. Nagayama 1), N. Ohyabu 1), H. Yamada 1), A. Komori 1), O. Motojima 1), and the LHD Experimental Group

1) National Institute for Fusion Science, Toki, Gifu 509-5292, Japan
2) Graduate School of Energy Science, Kyoto University, Uji, Kyoto 611-0011, Japan
3) Department of Nuclear Engineering, Kyoto University, Kyoto 606-8501, Japan

e-mail contact of main author: miyazawa@LHD.nifs.ac.jp

Abstract. The highest central density in net current free helical plasmas of 5×10^{20} m^{-3} has been demonstrated in the recent Large Helical Device (LHD) experiment. The volume-averaged electron density reaches 3×10^{20} m^{-3}, in spite of a small power density of less than 0.5 MW/m^3 and a magnetic field strength of less than 3 T. These are attained in the plasmas with strongly peaked density profiles generated by pellet injection. In the case of gas-fueled plasmas, complete detachment takes place when the hot plasma boundary shrinks below the last-closed-flux-surface (LCFS), or in other words, the edge temperature decreases to a critical value. The edge density that results in this shrinking corresponds to the maximum edge density achievable under the attached condition. At detachment, the ionization front moves from the ergodic region to inside of the LCFS and the particle confinement effectively improves. Under an appropriate recycling condition, complete detachment is self-sustained, which is called the Serpens mode. The discharge is finally terminated by radiating collapse, unless gas fueling is stopped. Radiating collapse is triggered even at a small radiation loss fraction of about 0.3, while it ranges from 0.3 to 1 at complete detachment. It is therefore difficult to determine a threshold radiation loss fraction that determines the operational density limit. Both of the critical densities for complete detachment and radiating collapse are dependent on the square root of the heating power, as is predicted by the conventional Sudo density limit scaling. This is explained by the edge temperature property that is a function of the square root of the heating power divided by the density, *i.e.* the density that results in a critical temperature increases with the square root of the heating power. Even though the Sudo fraction, which is the ratio of the volume-averaged density to the Sudo scaling, reaches as high as 3.5 in pellet-fueled plasmas, the edge density in these cases are similar to those in gas-fueled plasmas of which the Sudo fraction is ~0.8 at attachment. Indeed, the Sudo fraction is proportional to the peaking factor defined by the ratio of the volume-averaged density to the edge density, which exceeds 3 in pellet-fueled plasmas. In detached plasmas, edge densities are roughly twice as large as those in attached plasmas, reflecting the improved particle confinement.

1. Introduction

The operational density range in future magnetically confined deuterium-tritium fusion reactors will be of the order 10^{20} m^{-3} [1, 2]. Higher density is more favorable as long as the confinement property is maintained, since the fusion reaction rate increases with the density squared. Furthermore, high-density operation is effective to achieve *detachment* [3], which reduces the divertor heat load to permissible value for realistic materials, since the edge plasma temperature decreases due to dilution cooling together with enhanced radiation and charge-exchange losses at high-density.

High-density operation of the order 10^{20} m^{-3} has been carried out mainly in small or medium size devices, such as the Alcator C-Mod tokamak (C-Mod) [4], the Frascati Tokamak Upgrade (FTU) [5], and the Wendelstein 7-AS stellarator (W7-AS) [6]. Small plasma volume and resultant high heating power density in these small devices, and especially the high magnetic field strength up to 8 T in C-Mod and FTU are apparently helpful for high-density operation. In the case of W7-AS, high-density up to 4×10^{20} m^{-3} was attained with divertor

detachment, in spite of a low magnetic field strength of 2.5 T [6]. The heating power density was ≤ 4 MW/m^3 in W7-AS. In the Large Helical Device (LHD), on the other hand, the heating power density is less than 0.5 MW/m^3 and the magnetic field strength is less than 3 T, to date. To discuss a possibility of high-density operation in a future fusion reactor, it is necessary to construct a reliable operational density limit scaling that at least explains the experimental results of various existing devices.

The so-called *Sudo density limit scaling* [7] has been often used to discuss the operational density limit of helical plasmas. The Sudo scaling is defined by; n_c^{Sudo} (10^{20} m^{-3}) = 0.25 $(PB/(a^2R))^{0.5}$, where P (MW), B (T), a (m) and R (m) are the total heating power (P_{tot}), the magnetic field strength, the minor radius and the major radius, respectively [7]. It should be noted that strongly peaked density profiles are not in the scope of Sudo scaling. This scaling is based on the power balance between the heating power and the radiation loss that is proportional to n_e^2, where n_e is the electron density. In LHD, radiating collapse is triggered even at a small radiation loss fraction of ~30 % [8]. Sustainable complete detachment, named *the Serpens mode*, has been found in LHD [9]. The radiation loss fraction ranges from 30 to 100 % at complete detachment [10]. It is therefore difficult to determine a threshold radiation loss fraction that triggers radiating collapse. The temperature dependence of the thermal diffusivity changes from strong ($\chi_{eff} \propto T_e^{1.5}$, gyro-Bohm type) to weak ($\chi_{eff} \propto T_e^{0.5}$) at a density much less than the operational density limit [11], where T_e and χ_{eff} denote the electron temperature and the effective thermal diffusivity, respectively. The plasma stored energy is proportional to $\langle P_{dep}\rangle^{2/3} \langle n_e\rangle^{1/3}$ in the latter case (HD scaling [11]), where $\langle P_{dep}\rangle$ is the volume-average of the integrated heat deposition profile. It is necessary to use $\langle P_{dep}\rangle$ ($\sim P_{tot} \times \exp(-\langle n_e\rangle/12)$, for plasmas with a flat density profile at $\langle n_e\rangle > 3 \times 10^{19}$ m^{-3} [9]), to take into account the shallow penetration of the heating beams in high-density plasmas.

In this study, we experimentally investigate the operational density limit in LHD. Recent results of high-density experiments performed in LHD are given in Section 2. Density regimes for complete detachment and the operational density limit are also given. In Section 3, edge plasma parameters are highlighted to discuss plasma behavior in the vicinity of the operational density limit. A summary is given in Section 4.

2. High-density plasmas in LHD

2.1. Pellet-fueled plasmas

The highest volume-averaged density, $\langle n_e\rangle$, in LHD has reached 3×10^{20} m^{-3}, in the latest experimental campaign. Waveforms of the highest $\langle n_e\rangle$ discharge are depicted in FIG. 1. This was obtained at an *inward-shifted* configuration, where the magnetic axis, R_{ax} = 3.65 m and the magnetic field strength on the magnetic axis, B_0 = 2.71 T. Eight hydrogen ice pellets are injected from t = 0.7 to 1 s. Both the line-averaged electron density measured by a CO_2 laser interferometer, of which the line-of-sight passes through the core region of ρ = 0.06 (ρ is the normalized minor radius), and $\langle n_e\rangle$ measured by Thomson scattering reach 3×10^{20} m^{-3} at t ~ 1 s. Since the absolute sensitivity of each channel of Thomson scattering has not yet been calibrated, all Thomson density signals are multiplied by a single calibration factor to match $\langle n_e\rangle$ with that estimated from the Abel inversion of far-infrared (FIR) multi-chord interferometer signals. The electron density profile at the peak timing is shown in FIG. 2, together with the electron temperature and pressure profiles. The temperature profile becomes hollow transiently, just after the pellet injection that strongly peaks the density profile. The resultant pressure profile is flat in the core region of $\rho < 0.7$.

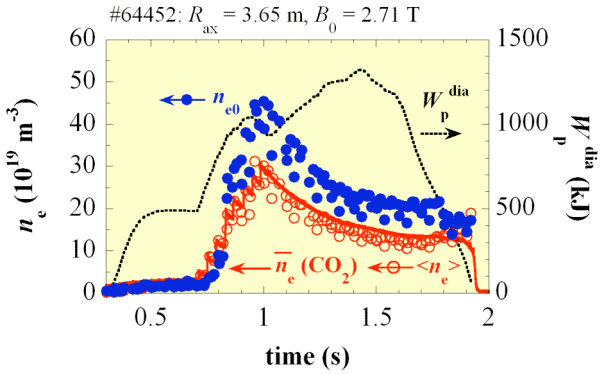

FIG. 1. Waveforms in a pellet fueled discharge that attains the highest volume-averaged density in LHD.

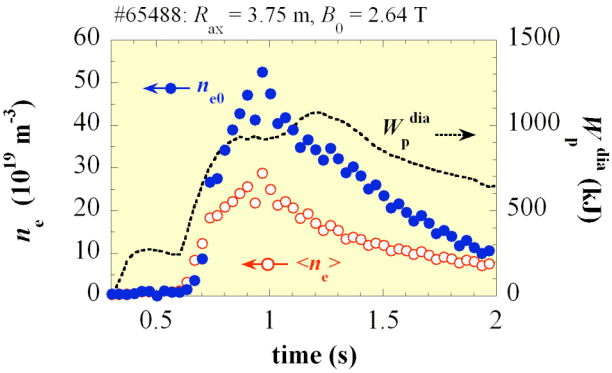

FIG. 3. Waveforms in a pellet fueled discharge that attains the highest central density in LHD.

The highest central density, n_{e0}, of 5×10^{20} m^{-3}, as shown in FIGs 3 and 4, was achieved at an *outward-shifted* configuration, where R_{ax} = 3.75 m and B_0 = 2.64 T. This is the world record in helical plasmas including heliotrons and stellarators. Hydrogen ice pellet injection was also used in this case. After the pellet injection, the electron density decreases and the electron temperature increases. The diamagnetic stored energy, W_p^{dia}, increases in this phase, as is known as *reheat*. In this case, the superdense core (SDC) [12] is formed after $t \sim 1.2$ s. Central plasma pressure reaches 100 kPa (the ion temperature, T_i, and the ion density, n_i, are assumed to be equal to T_e and n_e, respectively). This is also the world record in helical plasmas. A large Shafranov shift from 3.75 m to 4 m is observed at the SDC phase. Although SDC has been first found in the Local Island Divertor (LID) configuration [12], where $n_{e0} \sim 5 \times 10^{20}$ m^{-3} has also been attained, it is possible to form SDC in the usual helical divertor configuration, as in the case of FIGs 3 and 4.

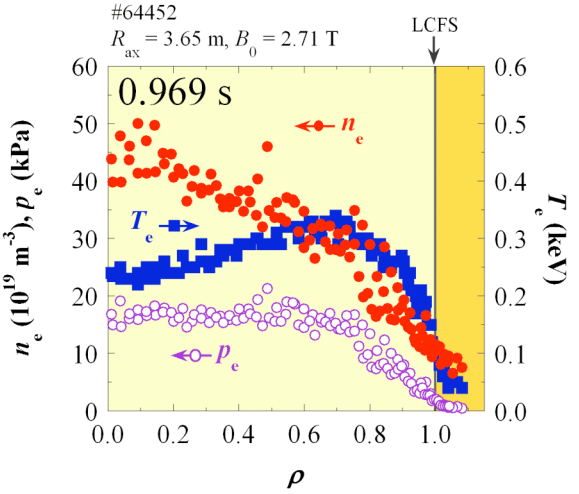

FIG. 2. Radial profiles of electron density, electron temperature, and electron pressure in the discharge shown in FIG. 1.

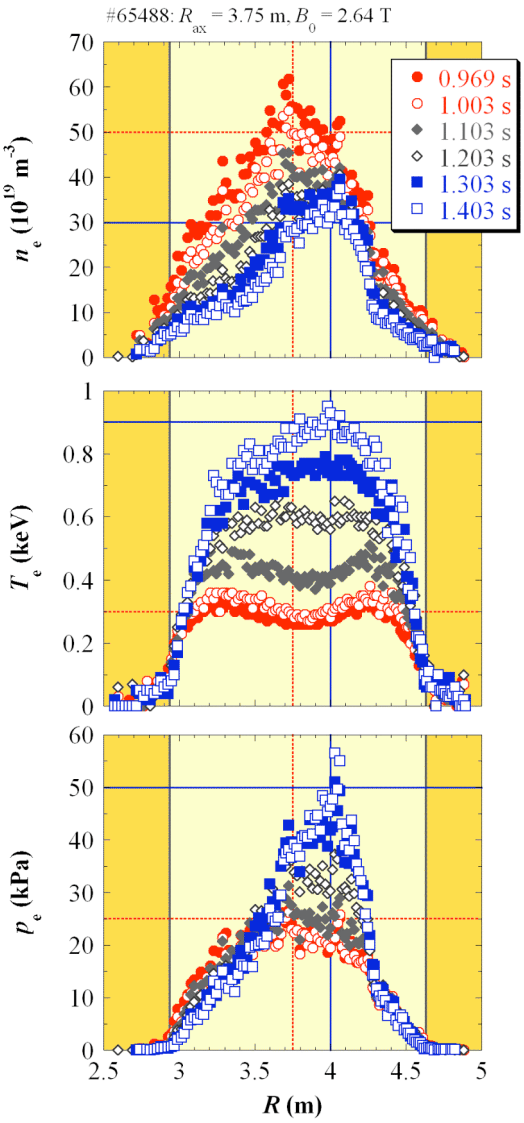

FIG. 4. Temporal evolution of radial profiles in the discharge shown in FIG. 3. The electron density, the electron temperature, and the electron pressure are shown from top to bottom.

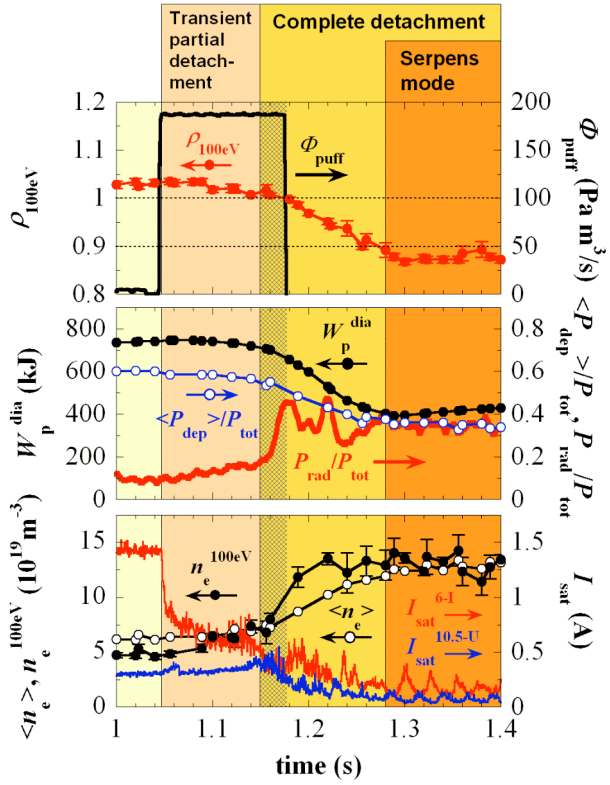

FIG. 5. Typical waveforms in a gas fueled high density discharge (shot #53614).

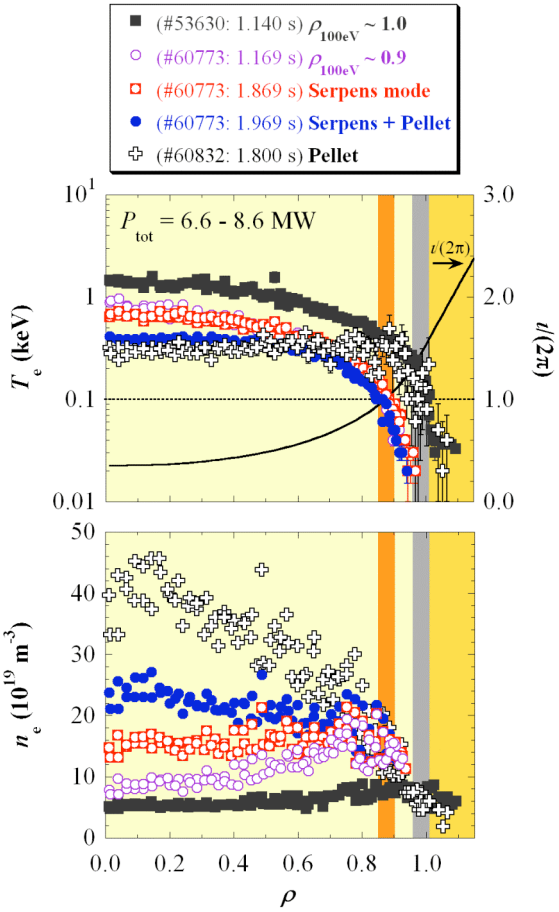

FIG. 6. Radial profiles of electron temperature (upper) and electron density (lower) in high-density discharges with various density peaking factors.

2.2. Gas-fueled plasmas

Detachment in LHD proceeds as in FIG. 5, where the density is increased by strong hydrogen gas puffing at a constant flow rate of $\Phi_{puff} \sim 200$ Pa m^3/s ($R_{ax} = 3.65$ m and $B_0 = 2.71$ T, $P_{tot} = 8.3$ MW). Then, the ion saturation current measured on the divertor tiles in the gas puff port, $I_{sat}^{6\text{-I}}$, decreases while it continues to increase with the density at the opposite side of the torus ($I_{sat}^{10.5\text{-U}}$). We refer to this as *transient partial detachment*. The hot plasma boundary, ρ_{100eV}, given as the normalized minor radius where $T_e = 100 \pm 50$ eV, gradually decreases during the transient partial detachment phase. The reason why ρ_{100eV} is highlighted as the hot plasma boundary will be explained in Section 3. When ρ_{100eV} decreases to 1, *complete detachment* takes place and I_{sat} begins to decrease at all the measured divertor tiles. In contrast to tokamaks, but similar to W7-AS, there are no clear indications of *high recycling* prior to detachment. The penetration of the heating beam becomes shallow and both $<P_{dep}>$ and W_p^{dia} decrease as $<n_e>$ increases. Nevertheless, W_p^{dia} is well reproduced by the HD scaling even at complete detachment [9]. As the edge T_e decreases, hydrogen volume recombination takes place [10] and the ionization front moves from the ergodic region to inside the last-closed-flux-surface (LCFS). The effective fueling efficiency for neutral particles is improved at complete detachment. This reflects the better particle confinement inside the LCFS, where particle diffusion perpendicular to the flux surfaces is important, compared with that in the ergodic region, where parallel particle transport through the open field lines dominates. Indeed, the density ramp up rate increases at $t \sim 1.15$ s in FIG. 5, even though Φ_{puff} is unchanged. To avoid an excess of density increase that leads to radiating collapse, it is necessary to decrease the fueling rate. Therefore, the density that results in $\rho_{100eV} = 1$ corresponds to the maximum density achievable under the attached condition. It is possible to increase the density further

beyond this critical density, under the completely detached condition. The Serpens mode begins when ρ_{100eV} decreases to ~0.9, and fluctuations due to a rotating helical radiation belt, named *the serpent*, appear in I_{sat}. In contrast to the Marfe observed in W7-AS, the serpent follows the magnetic field lines and is continuously propagating in both the poloidal and toroidal directions. In the Serpens mode phase, I_{sat} normalized by the main plasma density decreases to 10 % of the attached phase [9].

2.3. Density regimes of complete detachment and radiating collapse

Pellet injection is indeed effective to achieve a high-density. As is shown in FIG. 6, pellet-fueled plasmas are characterized by a strongly peaked density profile. In gas-fueled plasmas including detached and Serpens mode plasmas, the density profile is hollow or flat. However, even in pellet-fueled plasmas, edge densities are similar to those in gas-fueled plasmas. In FIG. 7, $\langle n_e \rangle$ and the edge electron density, n_e^{100eV}, given by the electron density at ρ_{100eV}, are plotted against P_{tot}, for the case of R_{ax} = 3.65 m and B_0 = 2.71 T. Shaded regions denote the density regimes for complete detachment. The n_c^{Sudo} plotted in FIG. 7 is calculated using the fixed parameters of $a = a_0$ = 0.64 m, $R = R_{ax}$ = 3.65 m, and $B = B_0$ = 2.71 T. High-density reaching 2.2 n_c^{Sudo} is sustainable in the Serpens mode plasmas. Higher densities as high as 3.5 n_c^{Sudo} are achieved by applying pellet injection, although these are transient. Even in these pellet-fueled plasmas, however, n_e^{100eV} are similar to those obtained in gas-fueled plasmas.

The high $\langle n_e \rangle$ achieved in pellet-fueled plasmas are the result of the strongly peaked density profiles, as shown in FIG. 8, where *Sudo fraction* defined by $\langle n_e \rangle / n_c^{Sudo}$ is plotted against a peaking factor defined by $\langle n_e \rangle / n_e^{100eV}$. In this case, n_c^{Sudo} is calculated using $a = a_0\ \rho_{100eV}$, to take into account the shrinking minor radius, while R = 3.65 m, and B = 2.71 T are fixed. The Sudo fraction linearly increases with the peaking factor, which exceeds 3 in pellet-fueled plasmas. In detached plasmas of which $\rho_{100eV} < 1$, n_e^{100eV} are larger than in the attached plasmas of which $\rho_{100eV} \sim 1$.

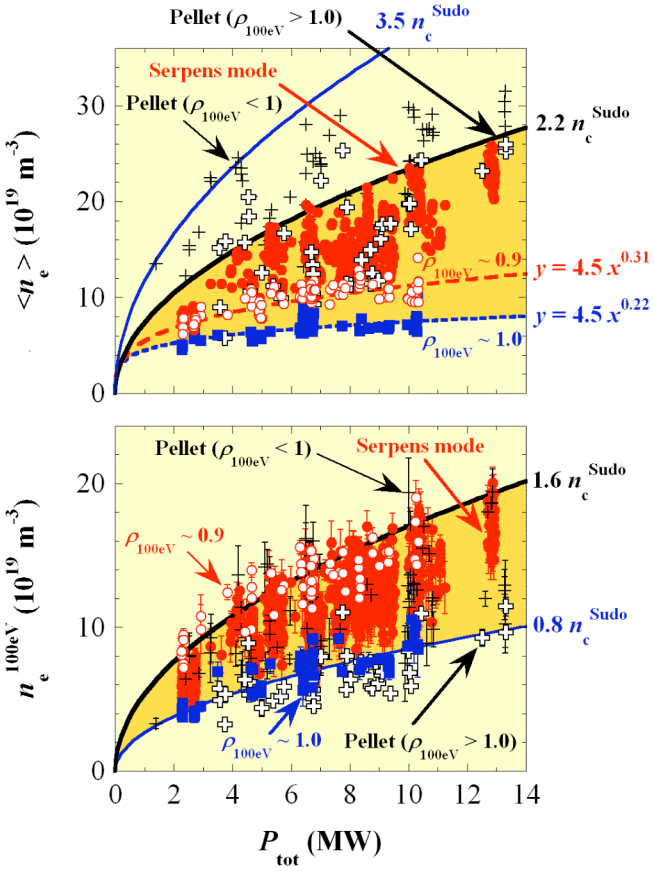

FIG. 7. The volume-averaged density (upper) and the edge density at the hot plasma boundary (lower) versus the total heating power.

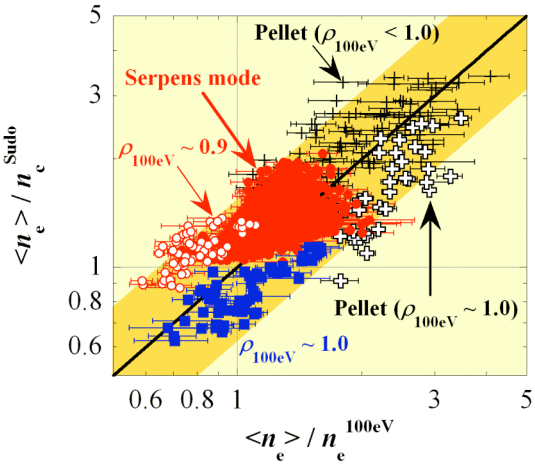

FIG. 8. Linear dependence of the Sudo fraction on the peaking factor.

3. Critical edge density

3.1. Electron temperature dependence on total heating power and density

As was mentioned in the introduction, the Sudo scaling is based on the power balance between P_{tot} and P_{rad} that is proportional to n_e^2, *i.e.* it is assumed that radiating collapse takes place at a critical radiation loss fraction of P_{rad} / P_{tot} $\propto$ n_e^2 / P_{tot}, and therefore, the critical density is proportional to $P_{tot}^{0.5}$. However, a large scatter of radiation loss fraction that ranges from 30 to 100 % at detachment suggests that this scenario is not sufficient to explain the density limit in LHD. Nevertheless, the threshold edge density for complete detachment does increase with $P_{tot}^{0.5}$ (see FIG. 7), as in the Sudo scaling. For a better understanding on this, the dependence of temperature on heating power and density is investigated.

The results of linear regression analysis of T_e for attached plasmas ($\rho_{100eV} > 1$) are summarized in FIG. 9, where the heating power and the density are scanned while the magnetic configuration is fixed to R_{ax} = 3.65 m and B_0 = 2.71 T. At each ρ, the local electron temperature, $T_e(\rho)$, is fitted by $n_e(\rho)^{\alpha n0}$ $P_{tot}^{\alpha P0}$, or $n_e(\rho)^{\alpha n1}$ $P_{dep}(\rho)^{\alpha P1}$, where $P_{dep}(\rho)$ is the total heating power deposited inside ρ, *i.e.* $P_{dep}(1.0) = P_{tot}$. Use of P_{dep} is effective to take into account shallow penetration of heating beams in high-density plasmas [11]. Since $P_{dep}(\rho) < P_{tot}$ inside the LCFS ($\rho < 1$), P_{tot} and $P_{dep}(\rho)$ give upper and lower estimation of the heating power, respectively. Note that $P_{dep}(\rho)$ is similar to P_{tot} in the very edge region of $\rho > 0.9$, and therefore both fitting results coincide in this region. The ratio of – αP0 / αn0 (or, – αP1 / αn1) is ~ 0.5 in the edge region and ~ 1 in the core region. This means that T_e can be expressed by a function of ($P_{tot}^{0.5}/n_e$) in the edge region, while T_e in the core region is expressed by another function of (P_{tot}/n_e). For example, T_e at ρ = 1 is well fitted by ($P_{tot}^{0.5}/n_e$)$^{2/3}$, as is shown in FIG. 10. This fitting fails, however, at T_e < 100 eV, suggesting that the heating power is lost by enhanced radiation in the low temperature regime, and/or the transport property changes. Although the reason why this occurs at T_e ~ 100 eV is not known and remains for future studies, the critical temperature scarcely depends on P_{tot} [8], at least under fixed conditions of the magnetic configuration, working gas, and wall conditioning.

Since the edge temperature is a function of ($P_{tot}^{0.5}/n_e$), the critical density that results in a critical temperature should be dependent on $P_{tot}^{0.5}$, as seen in FIG. 7 and in the Sudo scaling. In this explanation, the power balance between P_{tot} and P_{rad} is not mentioned explicitly. Nevertheless, this power balance might be playing an important role in determining the critical temperature.

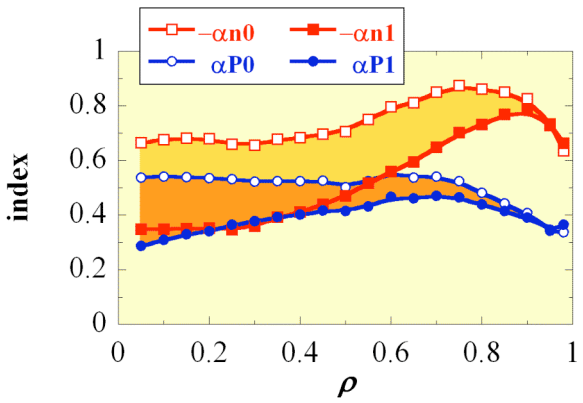

FIG. 9. Summary of regression analysis of the electron temperature in attached plasmas. See text for definition of fitting parameters.

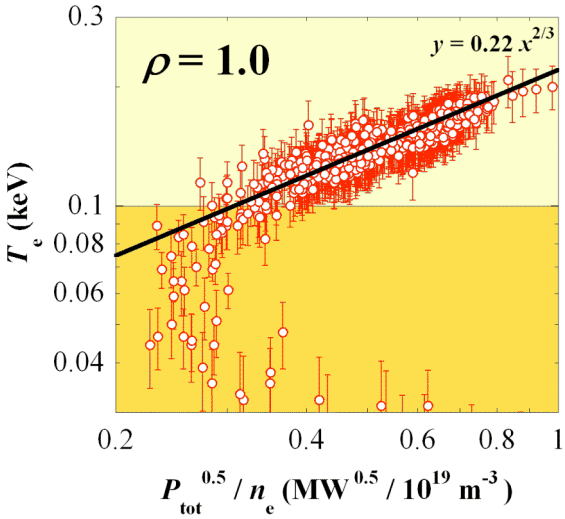

FIG. 10. Electron temperature dependence on the square root of heating power divided by the local electron density, at the LCFS.

3.2.Evolution of the edge density

At complete detachment, n_e^{100eV} begins to increase rapidly reflecting improvement of the effective fueling efficiency (see FIG. 5 in Section 2) and continues to increase toward radiating collapse, unless gas fueling is decreased. However, this increase of the edge density is only observed inside ρ_{100eV}. Outside of the hot plasma boundary ($\rho > \rho_{100eV}$), the density decreases as the plasma column shrinks, even though gas fueling is continued. In FIG. 11, shown are $n_e(\rho)$ / $P_{tot}^{0.5}$ at the fixed positions of ρ = 0.8, 0.9, and 1.0, in shrinking plasmas where ρ_{100eV} decreases from > 1 to zero (from right to left in FIG. 11). The local density at each ρ increases with decreasing ρ_{100eV}, as long as $\rho_{100eV} > \rho$, and begins to decrease with ρ_{100eV}, after ρ_{100eV} passes through the ρ. As a result, for example, the maximum density at ρ = 0.9 is obtained when $\rho_{100eV} \sim 0.9$, *i.e.* the maximum of $n_e(0.9)$ is roughly equal to n_e^{100eV} at ρ_{100eV} = 0.9. Therefore, n_e^{100eV} is a good representative of the maximum of $n_e(\rho)$ at each ρ. Now, the meaning of ρ_{100eV} as the hot plasma boundary can be redefined as below; ρ_{100eV} is the radial position inside which one can increase the electron density by fueling.

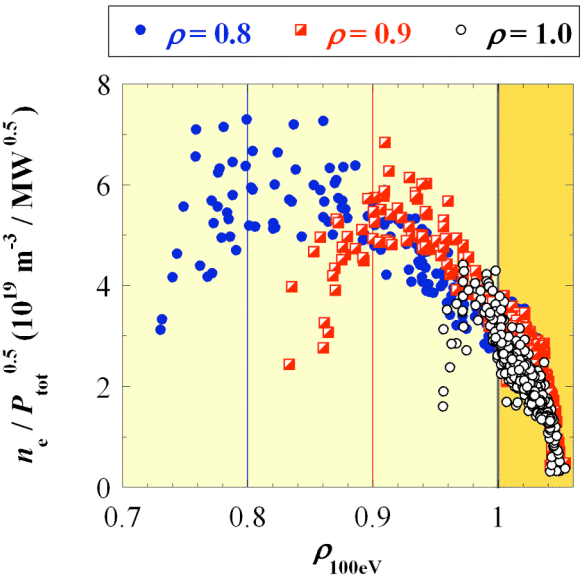

FIG. 11. Local densities normalized by the square root of total heating power, with respect to the hot plasma boundary.

3.3. Maximum edge densities achievable in attached and detached conditions

Since n_e^{100eV} represents the maximum local density and increases with $P_{tot}^{0.5}$, a plot of n_e^{100eV} / $P_{tot}^{0.5}$ versus ρ_{100eV}, as in FIG. 12, gives a radial profile of maximum edge densities in attached and detached plasmas. The maximum edge density increases as the plasma column shrinks and ρ_{100eV} decreases. In the attached condition ($\rho_{100eV} \geq 1$), therefore, the maximum is reached at ρ_{100eV} = 1, which roughly corresponds to 0.8 n_c^{Sudo} on average. As ρ_{100eV} decreases,

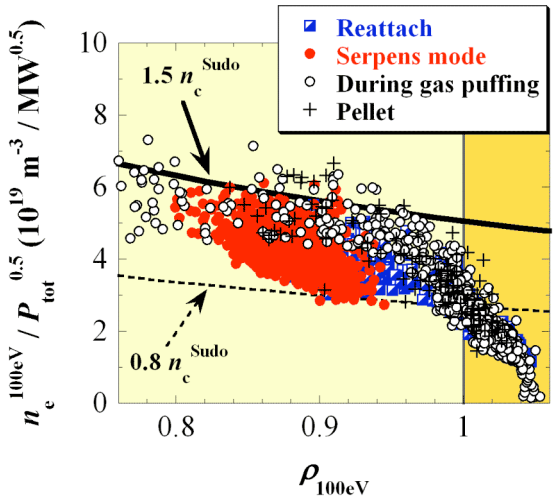

FIG. 12. Relation between the shrinking hot plasma boundary and the edge electron density normalized by the square root of total heating power.

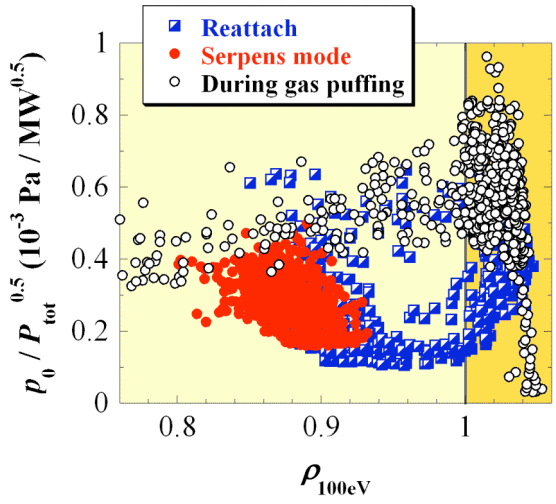

FIG. 13. Relation between the shrinking hot plasma boundary and the neutral pressure normalized by the square root of total heating power.

the maximum edge density increases further and then saturates to ~1.5 n_c^{Sudo} at $\rho_{100eV} \leq 0.95$. Even in the pellet-fueled plasmas (crosses in FIG. 12), the maximum edge density follows the same tendency as in gas-fueled plasmas (open circles). Note that this maximum edge density is not necessarily sustainable. To avoid further shrinking that leads to radiating collapse, one should decrease the fueling. Serpens mode appears in such a situation (closed circles). In the Serpens mode phase, ρ_{100eV} fluctuates within 0.8 to 0.95, and correspondingly, the maximum edge density also fluctuates within 1.5 n_c^{Sudo} to 0.8 n_c^{Sudo}. Even if the edge density decreases to 0.8 n_c^{Sudo}, which is the threshold density for complete detachment, the Serpens plasma keeps the detachment condition of $\rho_{100eV} < 1$. In some cases, however, the plasma does reattach after the Serpens mode phase.

In FIG. 13, shown are the neutral pressure, p_0, normalized by $P_{tot}^{0.5}$, versus ρ_{100eV} as in FIG. 12. Generally, p_0 increases with the density in attached plasmas. At detachment, p_0 decreases even though gas puffing is continued and the edge density increases. In the Serpens mode phase after the gas puff is turned off, p_0 decreases to as small as ~1/3 of that during gas puffing. With low *recycling* conditions, p_0 decreases further and reattachment occurs. On the contrary, if recycling is too high and p_0 does not decrease enough even after the gas puff is turned off, then ρ_{100eV} continues shrinking toward radiating collapse.

4. Summary

The highest central density in net current free helical plasmas, including heliotrons and stellarators, of 5×10^{20} m^{-3} has been demonstrated in LHD. The volume-averaged density reaches 3×10^{20} m^{-3}. These are attained in plasmas with strongly peaked density profiles generated by hydrogen ice pellet injection. Even in these pellet-fueled plasmas, edge densities are similar to those in gas-fueled plasmas with flat or hollow density profiles. Complete detachment takes place when the edge temperature at the LCFS decreases to a critical value of ~100 eV. In the edge region, the electron temperature is a function of the square root of the heating power divided by the electron density. Consequently, the critical edge density that results in complete detachment is proportional to the square root of the heating power, as is expressed in the Sudo scaling. The critical edge density roughly corresponds to 0.8 times the Sudo scaling. High volume-averaged densities reaching ~2.2 times the Sudo scaling are sustainable in the Serpens mode plasmas, where the edge density is limited to ~1.5 times the Sudo scaling. Fueling and recycling control is necessary to reproduce the Serpens mode, because an excess (a shortage) of neutral pressure leads to radiating collapse (reattachment).

Acknowledgement

This work is supported by NIFS budget code NIFS06ULPP517.

References

[1] LAWSON, J.D., Proc. Phys. Soc. (London) **B70** (1957) 6.
[2] SAGARA, A. *et al*., Nucl. Fusion **45** (2005) 258.
[3] PITCHER, C.S. and STANGEBY, P.C., Plasma Phys. Control. Fusion **39** (1997) 779.
[4] LIPSCHULTZ, B. *et al*., Phys. Rev. Lett. **81** (1998) 1007.
[5] FRIGIONE, D. *et al*., Nucl. Fusion **36** (1996) 1489.
[6] MCCORMICK, K. *et al*., Phys. Rev. Lett. **89** (2002) 015001.
[7] SUDO, S. *et al*., Nucl. Fusion **30** (1990) 11.
[8] PETERSON, B.J. *et al*., Plasma Fusion Res. **1** (2006) 045.
[9] MIYAZAWA, J. *et al*., Nucl. Fusion **46** (2006) 532.
[10] MIYAZAWA, J. *et al*., Plasma Fusion Res. **1** (2006) 026.
[11] MIYAZAWA, J. *et al*., Plasma Phys. Control. Fusion **48** (2006) 325.
[12] OHYABU, N *et al*., Phys. Rev. Lett. **97** (2006) 055002.